

Cite this: *J. Mater. Chem. A*, 2014, 2, 20338

## Structure defects in g-C<sub>3</sub>N<sub>4</sub> limit visible light driven hydrogen evolution and photovoltage†

Po Wu,<sup>ab</sup> Jiarui Wang,<sup>b</sup> Jing Zhao,<sup>b</sup> Liejin Guo<sup>\*a</sup> and Frank E. Osterloh<sup>\*b</sup>

Graphitic carbon nitride (g-C<sub>3</sub>N<sub>4</sub>) is a promising visible-light-responsive photocatalyst for hydrogen generation from water. As we show here, the photocatalytic activity of g-C<sub>3</sub>N<sub>4</sub> is limited by structure defects generated during the calcination process. Specifically we find that the photocatalytic hydrogen production rate from aqueous methanol is inversely related to the calcination temperature (520–640 °C). The highest activity of 0.301 mmol h<sup>-1</sup> g<sup>-1</sup> is observed for the sample prepared at the lowest processing temperature. Surface photovoltage (SPV) spectroscopy shows that the maximum photovoltage is reduced (from 1.29 V to 0.62 V) as the processing temperature is increased, in accordance with higher defect concentrations and faster electron–hole recombination. The defects also produce additional optical absorption in the visible spectra and cause a red shifted, weakened photoluminescence (PL). Based on the sub-gap signal in the SPV and PL spectra, defect energy levels are +0.97 V and -0.38 V (vs. NHE) in the band gap of the material. According to Fourier transform infrared (FTIR) spectra, the defects are due to amino/imino groups in the g-C<sub>3</sub>N<sub>4</sub> lattice.

Received 8th August 2014  
Accepted 16th October 2014

DOI: 10.1039/c4ta04100c

www.rsc.org/MaterialsA

### 1 Introduction

As a possible solution to the problems of rising energy demands and environmental pollution, photocatalytic water splitting has attracted much attention in recent decades.<sup>1,2</sup> Hydrogen evolved from the reaction is an environmentally friendly, carbon-neutral fuel.<sup>3</sup> However, the relatively high cost of photo-electrochemical/photocatalytic H<sub>2</sub> production from water still hinders practical applications. Thus the development of a cheap, stable and effective photocatalyst for this process is of great interest.<sup>4</sup> From the aspect of light absorption, nitrides should be better than the commonly studied oxide photocatalysts (such as TiO<sub>2</sub>),<sup>5</sup> due to smaller electronegativity of N and correspondingly smaller bandgaps ( $E_G$ ) of nitrides.<sup>6</sup> Graphitic carbon nitride (g-C<sub>3</sub>N<sub>4</sub>) has been shown viable for both hydrogen production and organic contaminant degradation under visible light irradiation.<sup>7,8</sup> Its photocatalytic activity can be improved in several ways.<sup>9–11</sup> Porous g-C<sub>3</sub>N<sub>4</sub> morphologies were found to provide a larger specific surface area and more reactive sites.<sup>12,13</sup> Metal/non-metal doping can improve the visible light absorption and adjust the band edges.<sup>14,15</sup> Co-condensation with organic reagents containing cyano/amino/

conjugated groups can regulate the density of states and photocatalytic activity.<sup>16,17</sup>

Overall, the use of g-C<sub>3</sub>N<sub>4</sub> as a light absorber for solar energy conversion is complicated by the lack of purification steps after the synthesis.<sup>18</sup> Due to the many intermediates (such as biuret, cyanuric acid, ammeline and ammelide) involved in the synthesis,<sup>19</sup> defects in the final product are inevitable. Presently, little information is available on the benefits or disadvantages of these defects for photocatalytic hydrogen production. Some defects may serve as recombination centres for photo-generated electrons or holes, while others could promote charge separation or facilitate charge transfer at the surface. Three previous studies have looked at the role of thermal defects in g-C<sub>3</sub>N<sub>4</sub>. In 2013, Xu *et al.* found that the photocatalytic activity of g-C<sub>3</sub>N<sub>4</sub> for hydrogen evolution first increases with the processing temperature (450–600 °C) and then decreases at 650 °C.<sup>18</sup> The weaker photoluminescence (PL) for the 600 °C annealed sample was taken as evidence for a low defect concentration in that sample. But this interpretation does not consider the commonly accepted role of defects as non-radiative recombination centers.<sup>20,21</sup> Moreover, PL spectra were found to be unaffected, which conflicted with the continuous red shift of the emission with the increasing processing temperature, as reported by Zhang *et al.*<sup>22</sup> Lastly, in 2014, Zhang *et al.* reported that the fluorescence lifetime of g-C<sub>3</sub>N<sub>4</sub> under 465 nm light excitation decreases due to the greater defect concentration in high temperature processed samples.<sup>23</sup> However, H<sub>2</sub> evolution activity was found to increase with the processing temperature and with the BET surface area and to decrease with e<sup>-</sup>/h<sup>+</sup> life times. Clearly, the issue of defects in g-C<sub>3</sub>N<sub>4</sub> warrants additional investigation.

<sup>a</sup>International Research Center for Renewable Energy, State Key Laboratory of Multi-Phase Flow in Power Engineering, Xi'an Jiaotong University, No. 28 West Xianning Road, Xi'an, Shaanxi, 710049, P. R. China. E-mail: lj-guo@mail.xjtu.edu.cn; Fax: +86 029 82669033; Tel: +86 029 82663895

<sup>b</sup>Department of Chemistry, University of California, Davis, One Shields Avenue, Davis, CA, 95616, USA. E-mail: fosterloh@ucdavis.edu; Tel: +1 530 754 6242

† Electronic supplementary information (ESI) available. See DOI: 10.1039/c4ta04100c

Here we employ a combination of surface photovoltage (SPV) spectroscopy, photoluminescence, UV-Vis, IR-spectroscopy and photocatalytic measurements to evaluate the role of thermal defects in  $g\text{-C}_3\text{N}_4$ . A reduction of the photocatalytic activity of  $g\text{-C}_3\text{N}_4$  with an increasing processing temperature is clearly observed. This is accompanied by reduced photoluminescence yield, and a red shift of the emission. SPV detects a monotonic loss of the photovoltage with an increasing processing temperature that is due to a reduction of photogenerated charge carriers and leads to lowering of the quasi-Fermi energy of the illuminated sample. Sub-gap photovoltage features and red-shifted PL emission peaks are due to defect energy levels at +0.97 V and -0.38 V (vs. NHE), *i.e.* in the middle of the band gap. Lastly, Fourier transform infrared spectra and chemical analysis identify these defects as amino/imino groups in the  $g\text{-C}_3\text{N}_4$  lattice. This study thus provides a direct link between thermal defects in  $g\text{-C}_3\text{N}_4$  and their detrimental effects on carrier life times, photovoltage, and photocatalytic activity. The identification of the energy levels and chemical nature of these defects is the first step toward controlling them, and toward improving the performance of  $g\text{-C}_3\text{N}_4$  for solar energy conversion.

## 2 Experimental

### 2.1 Chemicals

Chemicals were purchased from ACROS Organics (dicyandiamide DCDA 99.5+%), Aldrich (methanol 99.8+%) or Fisher Scientific (acetone 99.7+%, isopropanol 99.8+%), and used as received. Water was purified to the resistivity of 18 M $\Omega$  cm using an ultrapure water system (NANOpure Infinity).

### 2.2 Synthesis

Graphitic carbon nitride ( $g\text{-C}_3\text{N}_4$ ) was synthesized through a facile calcination process. In detail, the precursor (DCDA: 5 g) was added into a crucible with a cover, heated in a tubular furnace to 520 °C (D52), 550 °C (D55), 600 °C (D60) and 640 °C (D64) for 4 h, cooled to room temperature, and ground to powder in a ceramic mortar for at least 10 min.  $g\text{-C}_3\text{N}_4$  suspensions were made by adding 5 mg of  $g\text{-C}_3\text{N}_4$  into water (3 mL), followed by 1 h ultrasonication.

### 2.3 Characterizations

UV-Vis absorption spectra were recorded with a Thermo Scientific Evolution 220 UV-Vis spectrometer, using the thick films fixed on white polytetrafluoroethylene (PTFE) seal tape. Tauc plots were obtained through two formulae:  $R = 10^{-A}$  and  $F(R) = (1 - R)^2/(2R)$ , where  $A$ ,  $R$  and  $F(R)$  stand for absorbance, relative reflectance and Kubelka-Munk function, respectively.<sup>24,25</sup> Powder X-ray diffraction (XRD) patterns were measured with a Scintag XRD (Cu K $\alpha$ :  $\lambda = 0.154$  nm) at -45 kV and 40 mA, equipped with divergence (2 mm), scatter (4 mm), column scatter (0.5 mm), and receiving (0.2 mm) slits. Fourier transform infrared reflection (FTIR) spectra were obtained with the IR spectrometer (BRUKER-Alpha) and software (OPUS 6.5). Photoluminescence (PL) emission spectra were recorded with a

FluoroMax-P instrument. Surface photovoltage (SPV) measurements were performed by using a vibrating gold Kelvin probe (Delta PHI Besocke) mounted inside a home-built vacuum chamber ( $<5 \times 10^{-4}$  mbar). The spectra of the Xe lamp and monochromator configuration are shown in Fig. S3.† Thin films for SPV measurements were prepared by drop coating 0.1 mL of  $g\text{-C}_3\text{N}_4$  suspension on ITO (Indium Tin Oxide)-coated glass (*ca.* 1.0 cm<sup>2</sup>) at room temperature, followed by heating on a hot plate at 100 °C for 10 min. Films were illuminated with monochromatic light from a 175 W Xe lamp filtered through an Oriel Cornerstone 130 monochromator (light intensity range: 0.1–0.3 mW cm<sup>-2</sup>). The obtained SPV spectra were corrected by subtracting a dark scan background recorded prior to the light measurement. Photocatalytic H<sub>2</sub> evolution tests were performed by dispersing 30 mg of photocatalyst in 100 mL aqueous methanol solution (20 vol%). Irradiation was carried out in a quartz round bottom flask using light from a 300 W Xe arc lamp that was passed through a 400 nm long-pass filter (1 M NaNO<sub>2</sub>). The power at the flask surface was 380 mW cm<sup>-2</sup> as measured by a photometer (IL1400BL) equipped with a GaAsP detector. Before the H<sub>2</sub> evolution test, platinum (1.0 wt%) was first photodeposited *in situ* on the photocatalyst under full spectrum irradiation for 2 hours from H<sub>2</sub>PtCl<sub>6</sub>·6H<sub>2</sub>O. Then the solution was directly used for the photocatalytic reaction. The air-tight irradiation system connects a vacuum pump and a gas chromatograph (Varian 3800: 60/80 Å molecular sieve column and a thermal conductivity detector) to quantify the amount of gas evolved. Prior to irradiation, the flask was evacuated down to 60 torr and purged with argon gas three times to remove air. No H<sub>2</sub> evolution was detected in the absence of photocatalysts or/and visible-light irradiation.

## 3 Results and discussion

Various  $g\text{-C}_3\text{N}_4$  samples were synthesized by polymerization of dicyandiamide at different temperatures between 520 °C and 640 °C. The graphitic crystalline structure of the materials was confirmed by the characteristic XRD diffraction peaks at 27.5° and 13.1° (Fig. S1†).<sup>26</sup> Selected other properties are listed in Table 1. We find that the product yield is a sensitive function of the calcination temperature – the highest yields were obtained at 520 and 550 °C. With the increase of temperature, the yield reduced significantly, and became zero at 700 °C, implying complete thermal decomposition of  $g\text{-C}_3\text{N}_4$ .

The color of the samples and their UV-Vis absorption spectra (Fig. 1) depend on the calcination temperature. For all samples, the major absorption occurs below 450 nm, corresponding to the transition from the valence band (VB) to the conduction band (CB). Based on Tauc plots (Fig. 1 inset), the band gap for D52 and D55 is found at 2.88 eV, similar to previous studies.<sup>7,27</sup> For the D64 sample, the absorption edge is shifted to around 410 nm, suggesting a slightly enlarged band gap of 3.03 eV, and indicating a quantum size effect.<sup>28</sup> Indeed, XRD data (Fig. S1†) show a weaker (002) diffraction peak for the D64 sample, revealing the presence of smaller crystalline domains. From the Scherrer equation, the size of these domains is 6.40 nm, suggesting that the Bohr exciton radius in  $g\text{-C}_3\text{N}_4$  is on this length

Table 1 Yields, SPV maxima, PL maxima, PL width and activities of different samples

Sample	Temp. (°C)	Yield (wt%)	SPV max. (V)	PL max. (eV)	PL width (nm)	H <sub>2</sub> rate (μmol h <sup>-1</sup> g <sup>-1</sup> )
D52	520	28.5	-1.29	2.70	72	301
D55	550	28.0	-0.90	2.65	78	173
D60	600	15.8	-0.82	2.63	104	153
D64	640	7.4	-0.62	2.23	114	59
D67	670	2.4	—	—	—	—
D70	700	0	—	—	—	—

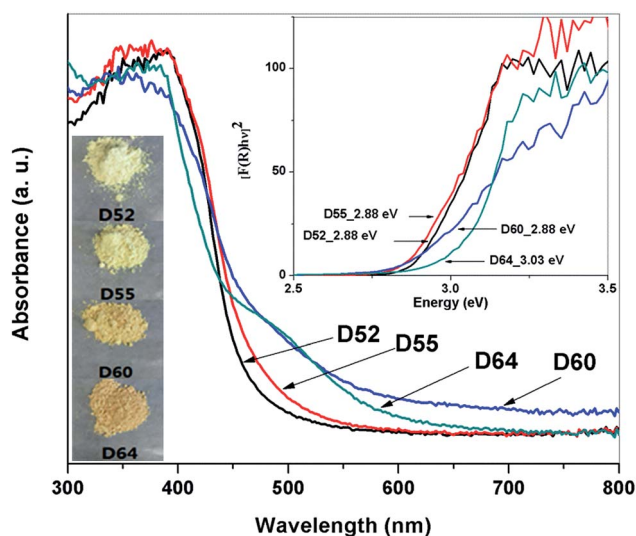


Fig. 1 Kubelka–Munk absorption spectra, photographs (the left inset) and Tauc plots (the right inset) of the as-synthesized samples D52, D55, D60 and D64.

scale. In addition, samples prepared at 600 and 640 °C have a new optical absorption shoulder at *ca.* 500 nm (2.48 eV). This shoulder is also responsible for the darker color of these samples (photographs in Fig. 1 inset). The absorption shoulder and the brown color are indicative of defects in g-C<sub>3</sub>N<sub>4</sub>, generated at a higher calcination temperature.

In order to test the activity of the samples for photocatalytic hydrogen evolution under visible-light, irradiation experiments were carried out on the suspended powders (30 mg) in aqueous methanol as the sacrificial agent (shown in Fig. 2). Prior to these tests, 1 wt% of Pt was deposited on the photocatalysts by photodeposition using the same procedure. During deposition, H<sub>2</sub> evolution rates became steady after one hour (Fig. S4<sup>†</sup>), indicating complete conversion of the precursor into Pt nanoparticles. Steady state evolution rates (Fig. 2 and Table 1) are between 301 μmol h<sup>-1</sup> g<sup>-1</sup> for D52 and 59 μmol h<sup>-1</sup> g<sup>-1</sup> for D64. Interestingly, the rates are inversely correlated with the g-C<sub>3</sub>N<sub>4</sub> preparation temperature (Fig. 2 inset). Meanwhile, all samples have the same sheet-like morphology (Fig. S5<sup>†</sup>), and the same Pt content and nanoparticle size (*ca.* 2 nm, Fig. S6<sup>†</sup>). This rules out variations in Pt coverage or g-C<sub>3</sub>N<sub>4</sub> morphology as the reason for the observed H<sub>2</sub> evolution trend in the platinized samples. Instead the activity of the photocatalysts appears to be

controlled by the defect concentration in the samples, and correspondingly by the steady state concentration of the photogenerated charge carriers.

Photoluminescence (PL) spectra can provide a measure of the carrier concentrations under illumination.<sup>20,21</sup> PL spectra obtained for the four samples are shown in Fig. 3. Under excitation at 350 nm, D52 produces a luminescence peak centred at 450 nm and with a full width at half maximum (FWHM) of 72 nm. The peak wavelength agrees well with the absorption edge of the material from UV-Vis absorption measurements. As the preparation temperature increases, the emission peak is red-shifted and increasingly broad (see Table 1). This trend agrees well with the observations by Zhang *et al.* for g-C<sub>3</sub>N<sub>4</sub> made from dicyandiamide.<sup>23</sup> The lower emission intensity can be attributed to increasing non-radiative recombination rates and shorter lifetime of the carriers,<sup>23,29</sup> while the shift to longer wavelength indicates the presence of sub-gap defects in the material. Interestingly, the temperature induced PL changes for g-C<sub>3</sub>N<sub>4</sub> synthesised by thermal condensation of urea are less pronounced.<sup>18</sup> In the urea system the luminescence yield does not decrease monotonically with temperature, and the observed red shift is less than 5 nm for samples made in the 550–650 °C temperature interval. The differences in these systems must be attributed to variable defect distributions resulting from the

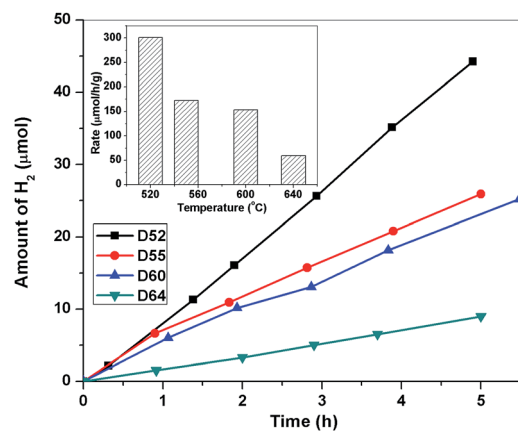


Fig. 2 H<sub>2</sub> evolution from samples (30 mg) in methanol (20 vol%) aqueous solution at pH = 4.5 under visible light (>400 nm) irradiation. Samples were platinized with 1% mass Pt prior to irradiation. Inset: relationship between the reaction rate and the calcination temperature.

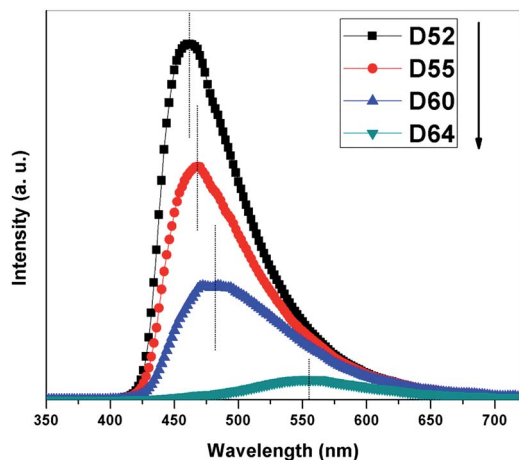


Fig. 3 PL spectra of the non-platinated samples as suspensions (excitation wavelength: 350 nm).

different  $g\text{-C}_3\text{N}_4$  formation pathways involving the urea or dicyandiamide reagents.

To further understand the role of defects in controlling the photocatalytic activity of  $g\text{-C}_3\text{N}_4$ , SPV spectra were recorded for each sample. SPV is a sensitive, wavelength dependent probe of light-driven charge separation in semiconducting materials.<sup>30–32</sup> It can provide information about the majority carrier type, band gap, defects, quasi-Fermi energy levels, and about charge transport in nanostructured materials.<sup>33,34</sup> In SPV, the surface potential of a sample film is detected contactlessly with a vibrating Kelvin probe. Fig. 4 shows SPV spectra of the four samples, together with the optical absorption spectrum for D52. All films produce a negative voltage, which means all  $g\text{-C}_3\text{N}_4$  samples are n-type semiconductors. This agrees well with previous SPV data from Dittrich *et al.* on  $g\text{-C}_3\text{N}_4$  powder obtained from cyanamide.<sup>35</sup> All the spectra consist of a minor

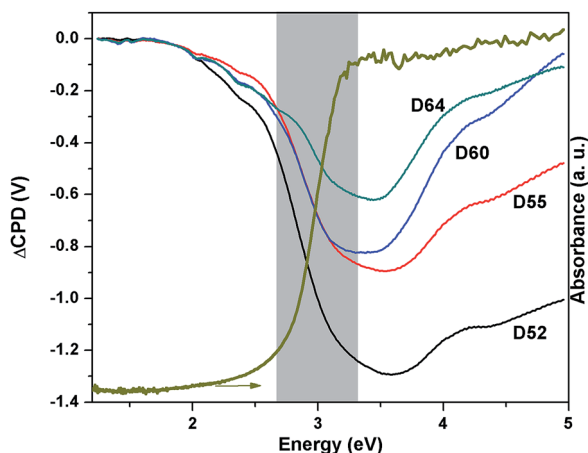


Fig. 4 SPV spectra of  $g\text{-C}_3\text{N}_4$  films (D52, D55, D60 and D64) on ITO substrate versus UV-Vis spectrum (dark yellow line) of D52. The grey bar represents the optical band gap of the material. The films were prepared using the same procedure to control the thickness (average 5  $\mu\text{m}$ ). The  $\Delta\text{CPD}$  fine structure at 2.05 and 2.35 eV results from the variable intensity of the light source (0.1–0.3  $\text{mW cm}^{-2}$ ).

$\Delta\text{CPD}$  signal at sub-gap photon energies 1.80–2.80 eV, a major signal at 2.80–3.50 eV, and a signal decay at energies  $>3.5$  eV. Based on the low excitation energy, the sub-gap feature is due to the excitation of mid-gap defect states. The main SPV signal is attributed to band gap excitation of  $g\text{-C}_3\text{N}_4$ , based on the overlap with the absorption edge. The maximum  $\Delta\text{CPD}$  signal is reached at 3.5 eV. At higher photon energy, the SPV signal decreases because the light is absorbed at the  $g\text{-C}_3\text{N}_4$  top layer and no longer reaches the bottom of the  $g\text{-C}_3\text{N}_4$  film. The spectra of the samples D52–D60 are similar, but there is a 0.20 eV blue shift in the band gap SPV signal for the D64 sample, which is also seen in the optical absorbance spectrum. It further confirms a quantum size effect in D64. Overall, the maximum  $\Delta\text{CPD}$  signal in the series is found to decrease monotonously with the increasing calcination temperature, with D52 at  $-1.29$  V, D55 at  $-0.90$  V, D60 at  $-0.82$  V and D64 at  $-0.62$  V.

This trend can be understood on the basis of the energy diagram in Fig. 5. For nanostructured films, the photovoltage is due to majority carrier injection into the substrate.<sup>33</sup> The theoretical voltage is controlled by the built-in potential of the  $g\text{-C}_3\text{N}_4\text{-ITO}$  junction, *i.e.* the difference between the quasi-Fermi level of the  $g\text{-C}_3\text{N}_4$  film (the donor), and the Fermi level of ITO (the acceptor). Based on literature values for the Fermi levels of ITO ( $+0.35$  V vs. NHE)<sup>36</sup> and  $g\text{-C}_3\text{N}_4$  ( $-1.20$  V vs. NHE at pH 6.6),<sup>37</sup> the built-in potential of the  $\text{C}_3\text{N}_4\text{-ITO}$  junction is  $-1.59$  V. Compared with this potential, the smaller experimental photovoltage indicates that the quasi-Fermi levels in the illuminated samples are more positive (Fig. 5) than the literature value. According to eqn (1),<sup>33</sup> this reflects a decrease of the steady state electron concentration  $n_e$  in the  $g\text{-C}_3\text{N}_4$  conduction band.

$$E_{F,n} = E_{CB} - kT \ln \frac{n_e}{N_{CB}} \quad (1)$$

Herein,  $k$ ,  $T$ ,  $E_{F,n}$ ,  $E_{CB}$ ,  $n_e$  and  $N_{CB}$  are the Boltzmann constant, temperature, quasi-Fermi level, conduction band minimum, electron concentration and effective density of states

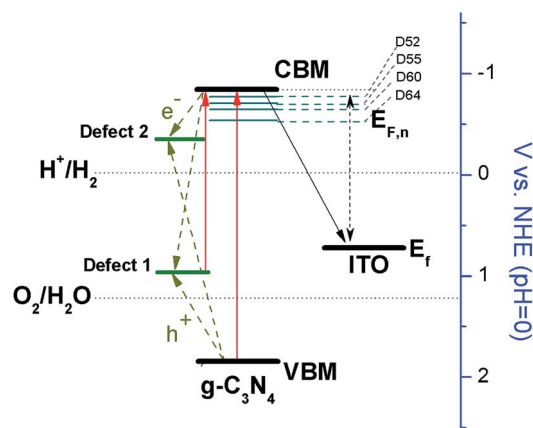


Fig. 5 Energy diagram of  $g\text{-C}_3\text{N}_4$  (CB:  $-0.83$  V; VB:  $+1.85$  V),<sup>37</sup> defect 1 ( $+0.97$  V), defect 2 ( $-0.38$  V) and ITO ( $+0.76$  V) with consideration of pH adjustment.<sup>36</sup>

in the conduction band, respectively. The decrease of  $n_e$  is a direct consequence of faster electron hole recombination resulting from the introduction of thermal defects. This trend follows the reduction of the PL emission intensity with increasing temperature. Based on the energy distribution of the PL emission peaks (460–472 nm for D52–D60, 556 nm for D64), there are two main defect types involved. The first one is tentatively placed at +0.97 V vs. NHE (see Fig. 5), based on the onset energy (1.80 eV) of the sub-gap photovoltage feature. It agrees with the ability of these states to catalyze electron hole recombination,<sup>38</sup> and to inject electrons into the substrate and generate a photovoltage under 1.80 eV excitation (see arrows in Fig. 5). For the D64 sample, an additional defect state is present near the conduction band. Excitation into this state causes no additional photovoltage, but leads to a broad absorption shoulder in the UV-Vis spectrum. Emission from these states is responsible for the PL shift to 556 nm. Meanwhile, the recombination at these states leads to further loss of the photovoltage and diminished  $g\text{-C}_3\text{N}_4$  reducing power ( $E_{F,n}$ ). Based on the PL emission peak of D64, the energy level of the second defect state is assigned to  $-0.38$  V vs. NHE (as shown in Fig. 5). It is interesting to compare our SPV results to those by Dittrich *et al.*<sup>35</sup> In that study, much smaller photovoltage values were measured (40–80 mV at 3.2 eV) and no sub-gap features were observed. These differences are likely a result of the lower built-in potential of the  $g\text{-C}_3\text{N}_4$ -carbon tape junction and of the lower intensity of the light source. A possible attenuation of the electric field from the argon matrix (higher dielectric constant) might have played an additional role.

In Fig. 6, we use Fourier transform infrared (FTIR) spectra to identify the structure of the defects involved in recombination. All spectra have the typical absorption bands of  $g\text{-C}_3\text{N}_4$ . The sharp peak at around  $800\text{ cm}^{-1}$  can be assigned to the breathing mode of the triazine units in  $g\text{-C}_3\text{N}_4$ .<sup>39</sup> In

addition, the bands observed in the region of  $1570\text{--}1634\text{ cm}^{-1}$  and  $1258\text{--}1480\text{ cm}^{-1}$  are the typical vibrations of  $\text{C}=\text{N}$  and  $\text{C}-\text{N}$  bonds, respectively, which belong to the skeletal stretching modes of aromatic rings.<sup>40</sup> However, close inspection of the spectra also reveals subtle differences among the products (shown with grey band and dashed lines), especially for those prepared at high temperature. To emphasize the trend, the FTIR spectrum of another sample, D67, prepared at  $670\text{ }^\circ\text{C}$  is also shown. Clearly, the absorption in the  $\text{N}-\text{H}$  stretching region between  $3000\text{ cm}^{-1}$  and  $3300\text{ cm}^{-1}$  becomes stronger, *i.e.* more  $-\text{NH}/\text{NH}_2$  groups are generated at a higher temperature.<sup>41</sup> This indicates a greater fraction of small polymer segments containing only a few heptazine units (5 units are shown in Scheme 1), and with  $-\text{NH}/\text{NH}_2$  groups at the terminals. This interpretation is supported by the increased splitting of the  $800\text{ cm}^{-1}$  band which can be assigned to individual heptazine and triazine rings.<sup>42</sup> As a result, the increased  $-\text{NH}/\text{NH}_2$  terminals in the small polymer segments are assigned to be the defects, which act as the recombination sites in the photocatalytic reactions. For D64 and D67, bands at  $1206\text{ cm}^{-1}$ ,  $1235\text{ cm}^{-1}$  and  $1316\text{ cm}^{-1}$  (grey region in Fig. 6) become more dominant. These bands can be associated with an increasing amount of  $\text{C}-\text{NH}-\text{C}$  bridges (shown in blue in Scheme 1) which result from linear linkage of heptazine units.<sup>18,41</sup> These units are likely candidates for the type 2 defects in  $g\text{-C}_3\text{N}_4$ . To verify these assignments, the ‘ninhydrin test’ was employed as an independent measure of the surface amine concentration in these samples. Ninhydrin (2,2-dihydroxyindane-1,3-dione) reacts with primary amines to produce a purple color known as ‘Ruhemann’s purple’, which can be detected by UV-Vis spectroscopy.<sup>43</sup> Absorption spectra of the test samples are shown in Fig. S7.† As can be seen, the intensity of the 570 nm dye absorption peak increases with the  $g\text{-C}_3\text{N}_4$  processing temperature, supporting increasing  $-\text{NH}_2$  surface concentrations in the series  $\text{D52} < \text{D55} < \text{D60}$ . However, D64 shows a weaker absorption at 570 nm. This means that the  $-\text{NH}_2$  groups have been replaced with less reactive  $-\text{NH}$  groups in the high temperature sample. This agrees well with the interpretation of the IR spectra.

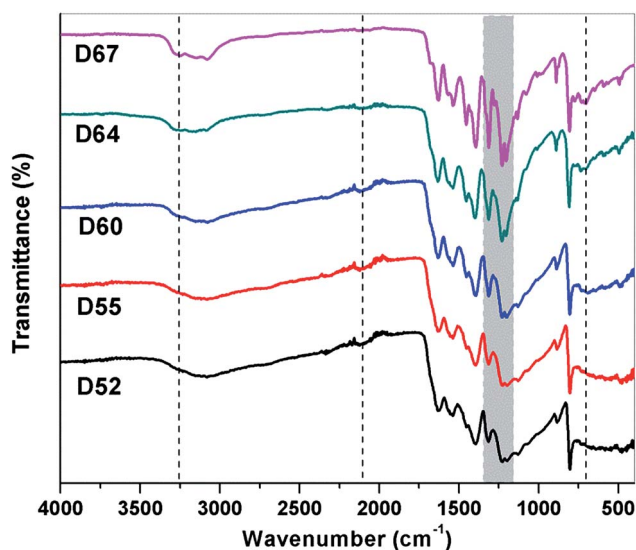
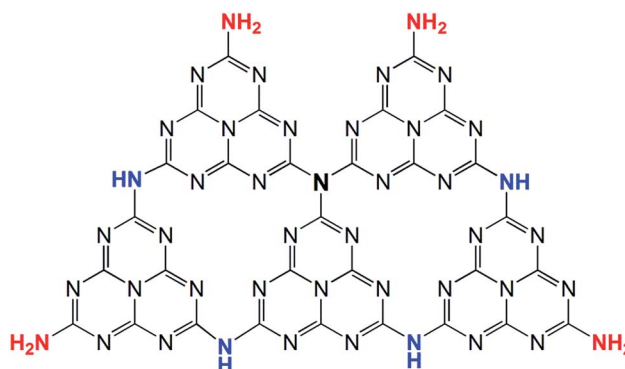


Fig. 6 FTIR spectra of the as-synthesized samples D52, D55, D60, D64 and D67. The grey band and dashed lines emphasize the differences. Spectra were normalized and stacked for comparison.



Scheme 1 Locations of  $-\text{NH}/\text{NH}_2$  groups in a segment with five heptazine units.

Finally, we note an impurity signal at  $2100\text{ cm}^{-1}$  in the IR spectra of samples prepared at low temperature. This band is assigned to the  $\text{-C}\equiv\text{N}$  group in DCDA (see also the Fig. S2†) and related intermediates.<sup>44</sup> This band gets weaker for D64 and D67, meaning there is less precursor (or intermediates) left in  $\text{g-C}_3\text{N}_4$  prepared at high temperature. Overall, these results suggest that there is a sensitive thermodynamic balance between incomplete polymerization of the precursor at low temperature, and the formation of  $\text{-NH/NH}_2$  trap sites at high temperature. This equilibrium and the lack of purification methods determine the defect concentration in  $\text{g-C}_3\text{N}_4$  and its photocatalytic performance.

## 4 Conclusions

In summary, we have shown that the photocatalytic hydrogen evolution activity of  $\text{g-C}_3\text{N}_4$  is limited by two types of defects whose energy levels can be assigned at  $+0.97\text{ V}$  and  $-0.38\text{ V}$  (vs. NHE), based on the sub-gap photovoltage signal, a red shifted optical absorption and reduced photoluminescence emission. The defects act as  $\text{e}^-/\text{h}^+$  recombination sites that reduce the free carrier concentration in illuminated  $\text{g-C}_3\text{N}_4$ . This depresses the photovoltage and reducing power (quasi-Fermi energy,  $E_{\text{F,n}}$ ) of the material. FTIR spectra and reactions with ninhydrin have identified the defects as amino/imino groups. Controlling these defects through alternate syntheses with different precursors, or under an inert atmosphere, or through chemical treatments will be key to improving the performance of the material for solar energy conversion.

## Acknowledgements

We are grateful for financial support from Research Corporation for Science Advancement (Scialog award) and from the National Science Foundation (NSF, CBET 1133099). This study was also sponsored by a scholarship from the State Scholarship Fund of the China Scholarship Council (CSC).

## Notes and references

- 1 K. Maeda, K. Teramura, D. Lu, T. Takata, N. Saito, Y. Inoue and K. Domen, *Nature*, 2006, **440**, 295.
- 2 F. E. Osterloh, *Chem. Soc. Rev.*, 2013, **42**, 2294–2320.
- 3 X. B. Chen, S. H. Shen, L. J. Guo and S. S. Mao, *Chem. Rev.*, 2010, **110**, 6503–6570.
- 4 A. Kudo and Y. Miseki, *Chem. Soc. Rev.*, 2009, **38**, 253–278.
- 5 J. Zhang, Y. Wu, M. Xing, S. A. K. Leghari and S. Sajjad, *Energy Environ. Sci.*, 2010, **3**, 715–726.
- 6 P. Wu, J. Shi, Z. Zhou, W. Tang and L. Guo, *Int. J. Hydrogen Energy*, 2012, **37**, 13704–13710.
- 7 X. Wang, K. Maeda, A. Thomas, K. Takanabe, G. Xin, J. M. Carlsson, K. Domen and M. Antonietti, *Nat. Mater.*, 2009, **8**, 76–80.
- 8 Y. Yang, Y. Guo, F. Liu, X. Yuan, Y. Guo, S. Zhang, W. Guo and M. Huo, *Appl. Catal., B*, 2013, **142**, 828–837.
- 9 Y. Zheng, J. Liu, J. Liang, M. Jaroniec and S. Z. Qiao, *Energy Environ. Sci.*, 2012, **5**, 6717–6731.
- 10 Y. Wang, X. Wang and M. Antonietti, *Angew. Chem., Int. Ed.*, 2012, **51**, 68–89.
- 11 F. E. Osterloh, *J. Phys. Chem. Lett.*, 2014, **5**, 2510–2511.
- 12 X. Wang, K. Maeda, X. Chen, K. Takanabe, K. Domen, Y. Hou, X. Fu and M. Antonietti, *J. Am. Chem. Soc.*, 2009, **131**, 1680–1681.
- 13 Y. Wang, X. Wang, M. Antonietti and Y. Zhang, *ChemSusChem*, 2010, **3**, 435–439.
- 14 X. Chen, J. Zhang, X. Fu, M. Antonietti and X. Wang, *J. Am. Chem. Soc.*, 2009, **131**, 11658–11659.
- 15 G. Liu, P. Niu, C. Sun, S. C. Smith, Z. Chen, G. Q. Lu and H.-M. Cheng, *J. Am. Chem. Soc.*, 2010, **132**, 11642–11648.
- 16 J. Zhang, G. Zhang, X. Chen, S. Lin, L. Möhlmann, G. Dołęga, G. Lipner, M. Antonietti, S. Blechert and X. Wang, *Angew. Chem.*, 2012, **124**, 3237–3241.
- 17 Y. Chen, J. Zhang, M. Zhang and X. Wang, *Chem. Sci.*, 2013, **4**, 3244–3248.
- 18 J. Xu, Y. Li, S. Peng, G. Lu and S. Li, *Phys. Chem. Chem. Phys.*, 2013, **15**, 7657–7665.
- 19 P. M. Schaber, J. Colson, S. Higgins, D. Thielen, B. Anspach and J. Brauer, *Thermochim. Acta*, 2004, **424**, 131–142.
- 20 A. D. Yoffe, *Adv. Phys.*, 2001, **50**, 1–208.
- 21 C. Bullen and P. Mulvaney, *Langmuir*, 2006, **22**, 3007–3013.
- 22 Y. Zhang, Q. Pan, G. Chai, M. Liang, G. Dong, Q. Zhang and J. Qiu, *Sci. Rep.*, 2013, **3**, 1943.
- 23 H. Zhang and A. Yu, *J. Phys. Chem. C*, 2014, **118**, 11628–11635.
- 24 P. Kubelka and F. Munk, *Z. Tech. Phys.*, 1931, **12**, 593–601.
- 25 J. Shi, L. Ma, P. Wu, Z. Zhou, J. Jiang, X. Wan, D. Jing and L. Guo, *ChemCatChem*, 2012, **4**, 1389–1396.
- 26 J. Chen, S. Shen, P. Guo, P. Wu and L. Guo, *J. Mater. Chem. A*, 2014, **2**, 4605–4612.
- 27 S. Datta and K. L. Narasimhan, *Phys. Rev. B*, 1999, **60**, 8246–8252.
- 28 A. P. Alivisatos, *Science*, 1996, **271**, 933–937.
- 29 A. Luque, A. Martí, E. Antolín and C. Tablero, *Phys. B*, 2006, **382**, 320–327.
- 30 L. Kronik and Y. Shapira, *Surf. Sci. Rep.*, 1999, **37**, 1–206.
- 31 L. Kronik and Y. Shapira, *Surf. Interface Anal.*, 2001, **31**, 954–965.
- 32 J. Lagowski, *Surf. Sci.*, 1994, **299**, 92–101.
- 33 J. Zhao and F. E. Osterloh, *J. Phys. Chem. Lett.*, 2014, **5**, 782–786.
- 34 D. Gross, I. Mora-Seró, T. Dittrich, A. Belaidi, C. Mauser, A. J. Houtepen, E. D. Como, A. L. Rogach and J. Feldmann, *J. Am. Chem. Soc.*, 2010, **132**, 5981–5983.
- 35 T. Dittrich, S. Fiechter and A. Thomas, *Appl. Phys. Lett.*, 2011, **99**, 084105.
- 36 F. E. Osterloh, M. A. Holmes, J. Zhao, L. Chang, S. Kawula, J. D. Roehling and A. J. Moulé, *J. Phys. Chem. C*, 2014, **118**, 14723.
- 37 J. Zhang, X. Chen, K. Takanabe, K. Maeda, K. Domen, J. D. Epping, X. Fu, M. Antonietti and X. Wang, *Angew. Chem., Int. Ed.*, 2010, **49**, 441–444.
- 38 P. Würfel, *Physics of Solar Cells*, Wiley-VCH, Weinheim, 2005.
- 39 M. J. Bojdys, J.-O. Müller, M. Antonietti and A. Thomas, *Chem.-Eur. J.*, 2008, **14**, 8177–8182.

- 40 S. Martha, A. Nashim and K. M. Parida, *J. Mater. Chem. A*, 2013, **1**, 7816–7824.
- 41 B. V. Lotsch, M. Döblinger, J. Sehnert, L. Seyfarth, J. Senker, O. Oeckler and W. Schnick, *Chem.–Eur. J.*, 2007, **13**, 4969–4980.
- 42 B. V. Lotsch and W. Schnick, *Chem.–Eur. J.*, 2007, **13**, 4956–4968.
- 43 R. McGrath, *Anal. Biochem.*, 1972, **49**, 95–102.
- 44 A. J. Belsky and T. B. Brill, *J. Phys. Chem. A*, 1998, **102**, 4509–4516.